Air entrainment in the primary impact of single drops on a free liquid surface

Air entrainment in the primary impact of single drops on a free liquid surface

E Salerno[1], P Levoni[1,2] and G S Barozzi[1]

[1] DIEF- Dipartimento di Ingegneria "Enzo Ferrari", Università di Modena e Reggio Emilia, Via Vivarelli 10 - 41125 Modena (Italy)
[2] MIMESIS fluid dynamics & energy, Strada Contrada 309 - 41126 Modena (Italy)

Email: elisabetta.salerno@unimore.it

Abstract. Air-bubble entrainment produced by the impact of water drops on a liquid pool is investigated with the use of high-speed imaging. A wide range of drop volumes and impact velocities is considered to determine how the entrainment mechanisms change with varying the impact conditions. Five different entrainment regimes are distinguished on the basis of the observed flow phenomena. Their characteristic features are described in terms of bubble formation, crater evolution, jetting and secondary drop ejection. A regime map is reconstructed in the Froude-Weber space. Results obtained in the present study show good agreement with the phase diagrams reported in the literature and contribute to complete the scenario of the entrainment regimes. Quantitative data about the size and the residence times of the entrained nuclei are also presented.

1. Introduction

The impact of drops on a liquid surface often results in the introduction of gaseous nuclei in the receiving medium. This phenomenon is encountered in a large variety of natural and technological processes. In some applications, such as marine and climate science [1], nucleate boiling [2, 3] and fire suppression systems [4], the entrainment of bubbles can have positive implications since it promotes the transfer of heat and the exchange of gas molecules across the liquid-gas interface. On the contrary, the inclusion of bubbles is an undesirable phenomenon in filling and pouring processes, like the industrial handling of molten metals [5], cosmetic and pharmaceutical preparations [6] and liquid foods [7]. In those fields, highly perturbed filling jets are usually employed, which tend to disrupt into discrete droplets due to instabilities. The consequent entrainment of air resulting from the drops impinging on the free surface is detrimental to the product quality and production rates, as bubbles can cause defects, produce chemical and biological instabilities or give rise to foam.

In any case, it is of crucial importance to define the conditions for which entrainment occurs as well as understand the incidence of the phenomenon in quantitative terms. For these reasons, the impact of drops has been largely investigated in the last decades. In particular, the recent improvements in high-speed imaging techniques have allowed a better insight into these rapidly evolving events, leading to the identification of different mechanisms of entrainment. They can be summarized as follows.

In the case of drops falling on a deep pool of liquid at relatively low impact velocities, Thoroddsen et al. [8] and Tran et al. [9] showed that a thin hemispheric layer of air remains entrained between the two liquid bodies at the very beginning of the impact process. This layer prevents the immediate

coalescence of the drop, and its subsequent draining out and rupture lead to the production of hundreds or thousands of micron-sized bubbles within a few of milliseconds. According to the energy of impact, rupture can occur once the entrained layer is completely stretched or can start before it has drained out. The so-called "Mesler entrainment" [2, 3] is obtained in the latter case. When the kinetic energy of the drop is sufficiently high, a thin disk of air remains enclosed rather than a hemispherical cap [10], whose contraction usually results in the formation of a pair of nuclei. These nuclei are often referred to as "Thoroddsen bubbles" and have diameters ranging from tens to hundreds of microns. Accompanying their appearance, a multitude of smaller nuclei arranged in a ring distribution can be observed [10, 11]. As it was first postulated by Oguz and Prosperetti [12], these additional nuclei derive from the evolution of the outer contact line between the drop and the pool surface.

Soon after contact is established, a deep crater may be created in the receiving liquid as the drop impact energy is converted into potential and surface energy of the fluid. When the crater collapses under the action of the surrounding liquid, a portion of air can be left behind and other forms of entrainment are obtained. In some cases a single large bubble detaches from the bottom of the crater. Such a scenario is the result of a delicate balance between the motion reversal of the cavity walls, which starts at different times in different positions, and the convergence of capillary waves at the bottom of the crater [13–15]. With high-energy impacts, surface tension-driven instabilities develop on the base of the crater and several bubbles of smaller size appear.

The conditions of occurrence of the cited entrainment mechanisms are usually reported in terms of non-dimensional parameters. When water is used as the working fluid, the Weber and the Froude numbers are assumed sufficient to describe the impact problem; these are defined as $We = \rho V^2 d / \gamma$ and $Fr = V^2 / gd$, respectively. Here, d is the drop diameter, V the impact velocity, g the gravitational acceleration, ρ the density, and γ is the surface tension of the liquid. The existing studies on air entrainment in deep pools cover a limited number of impact conditions or refer to single stages of the impact process. The majority of data available in the literature concerns the production of single large bubbles by crater collapse. This form of entrainment has been observed to occur repeatedly and predictably in a well-defined region of the Froude-Weber space. For this reason, this mechanism is called "regular entrainment". The lower and upper limits of the regular entrainment regime were determined by Oguz and Prosperetti [13] and are expressed by the power law equations $We = 41.3Fr^{0.179}$ and $We = 48.3Fr^{0.247}$. Out of these boundaries, the process of single bubble formation can still be achieved, though it is no longer reproducible. For Weber and Froude numbers above the upper limit of regular entrainment region, slight differences in the crater dynamics may lead to different forms of entrainment. These types of entrainment regimes are still poorly investigated [11, 14, 16–18]. The definition of the Froude and Weber numbers delimiting the occurrence of the entrainment phenomena due to air film rupture is also quite controversial. According to the observations of Liow [18], the hemispherical cap is not formed when $Fr < 7$ and $We = Fr$. Liow and Cole [11] found values for the Weber number ranging from 6 to 20 for the case of Mesler entrainment, and $We < 6$ for film rupture after complete drainage. At $We > 20$, Thoroddsen bubbles and Oguz-Prosperetti bubble rings may appear [10, 11]. No dependence on the Froude number has been reported relative to these phenomena.

It must be pointed out that the quantitative limits discussed here are valid only for the case of liquids with low viscosity. When viscosity effects cannot be neglected a third dimensionless quantity is required to properly characterize drop impacts. This is usually written in the form of the capillary number Ca ($Ca = \mu V / \gamma$, where μ is the liquid viscosity). For what concerns the production of bubbles by cavity collapse, the global role of viscosity is seen as a damping of the capillary waves propagating along the crater walls, and a weakening of the crater reversal dynamics. This reflects in an increase of the inviscid regular entrainment limits in the Fr-We space [15]. On the other hand, the exact influence of liquid viscosity on the onset of bubble production by air film rupture has not yet been clarified.

From the above considerations it is evident that, despite the progress made so far in the study of the impact process, the global picture is still not exhaustive. The purpose of this research is to obtain a more complete scenario of the entrainment phenomena. To this aim, a series of practical experiments

involving water drops impinging on a deep pool of the same liquid was carried out. A wide range of drop volumes and falling heights was explored. High-speed imaging was adopted both to examine the impact dynamics, and to follow the process evolution over long time scales. The recorded image sequences were analysed and a regime map was reconstructed, based on the measured impact conditions. The size and the residence time of the bubbles were also extracted from the images, in order to offer useful indications about the role of bubble entrainment in practical processes.

2. Experimental procedures

2.1. Drop generation and receiving system

As sketched in figure 1, the experimental apparatus used in this work for the study of drop impacts consists of two main sections: i) the drop generation and receiving system, and, ii) the imaging system.

For the generation of the liquid drops, a positive displacement dispensing pipette was adopted. A 12 Volt DC motor, manually activated through a switch, was employed to control drop release and generate drops of different size. Drop volumes ranging from 2 to 23 µl were obtained with this facility. The pipette was suspended above a large rectangular glass tank containing the receiving liquid, and having a base area of 220 x 400 mm and a height of 250 mm. In order to make negligible the influence of the tank walls on the impact dynamics, a minimum lateral distance of 110 mm was always maintained between the syringe tip and the tank sidewalls. Similarly, bottom effects were excluded by filling the tank up to a height of 150 mm. To observe the influence of different falling heights, the pipette was mounted vertically on a traversing arm, capable of 0.1 mm minimum displacements in the three orthogonal directions. Ten different heights for the syringe tips were selected, ranging from 30 to 300 mm relative to the pool free surface. About 16 drop impacts were examined for each falling height, for a total of 176 trials.

Deionized water was used as the working fluid for both the drops and the liquid pool. To avoid surface contamination by large dust particles from the external ambient, in the course of the experiments the tank was covered with a transparent acrylic sheet, just leaving free the passage for the falling drop. At the end of each experimental series, the liquid inside the pool was removed and replaced with fresh fluid. Since the pool temperature could vary in the course of the experiments, due to intense illumination, a resistance thermometer was introduced in the liquid pool. Variations in the physical properties of the liquid, i.e. surface tension and density, could thus be accounted for. Throughout the entire set of experiments, a maximum temperature excursion of 6.8 °C was recorded, from a minimum of 15.6 °C up to 22.4 °C.
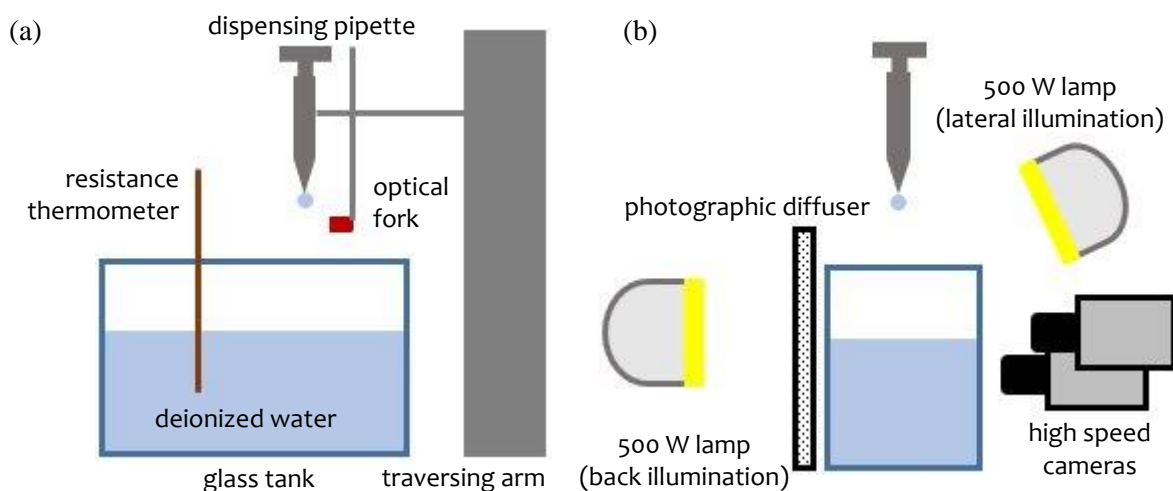

Figure 1. Schematic of the experimental apparatus: front view of the drop generation and receiving system (a), and side view of the imaging system (b).

High-speed imaging was adopted for the recording of the impact events. A pair of NanoSense MkIII CMOS cameras from Dantec Dynamics was arranged in front of the pool, for the simultaneous observation of the flow phenomena below and above the pool free surface. Both the cameras were fitted with a Micro Nikkor 60 mm f/2.8 lens. Magnifications of 36 and 23 μm/pixel were obtained for the camera focused on the falling drops, and the camera focused below the pool free surface, respectively.

The acquisition rate was varied from impact to impact in order to observe phenomena characterized by different time scales. The minimum acquisition rate of 100 fps was set to get information about the residence times of the entrained bubbles. On the other hand, framing rates up to 3600 fps were achieved by reducing the image resolution, so as to follow the impact dynamics with high temporal resolution. The acquisition start was triggered by means of an optical fork sensor, located just below the syringe tip for the detection of the falling drop. When the drop intercepts the light beam, generated by an infrared LED source, the reflected light is detected by a phototransistor and a TTL signal is sent to the cameras to initiate recording. The microcontroller Arduino Uno was employed for the generation of signals, whose rate was verified with the use of an oscilloscope. A maximum synchronization error of 6.6 μs was measured, including the contribution of the cables. Two 500 W halogen lamps were used as the light sources. One of them was placed behind the impact site to provide back illumination. A photographic diffuser was interposed between the lamp and the pool backside, so producing a uniform distribution of the emitted light. The second lamp provided additional lateral illumination.

2.2. Data reduction

The extrapolation of quantitative information on the impact phenomena was performed by processing the acquired images with the software ImageJ (provided by NIH, USA).

The image sequences related to the fly of the drops before impact were analysed to obtain the drop diameter and the impact velocity. In the presence of large three-dimensional drop oscillations after release, the frame exhibiting the less deformed drop shape was processed for the estimate of the drop size. Each drop was approximated with an ellipsoid, from whose volume the equivalent spherical diameter was evaluated. Drop diameters ranging from 1.55 to 3.54 mm were measured. For deformed drops, a maximum relative variation Δd of 9% resulted between the two axes of the ellipsoid. In the majority of cases, however, the shape variation was far below this value.

The impact velocity was derived from the last frames of the drop falling sequence: the coordinates of the centroid were tracked and their shift was then divided by the time interval between frames. The measured horizontal velocity at the impact position was less than 4% of the vertical velocity, indicating that all drops fell almost orthogonally on the pool free surface. The impact velocity range explored in the experiments was estimated to lie between 0.52 and 2.41 m/s.

The measured values of the drop diameter and the impact velocity were later used to calculate the Weber and the Froude numbers for the characterization of the impact conditions. Weber numbers ranging from 10 to 270 and Froude numbers between 8 and 329 were obtained. Considering the maximum uncertainty of drop size and impact velocity, of 1% and 3%, respectively, the accuracy of the Weber and the Froude number was estimated to be of at least 7%.

3. Results and discussion

3.1. Entrainment regimes

The analysis of the impact sequences recorded above and below the pool free surface led to the identification of five different entrainment regimes corresponding to different impact conditions. In the following subsections, the various regimes are presented and discussed for increasing values of We and Fr.

3.1.1. Initial contact I regime. For low Weber and Froude numbers, the sole entrainment mechanism involved in the impact process is the formation of small air bubbles as the drop first comes into contact with the pool surface. Hence, this regime has been denoted as "*initial contact I*". Those bubbles become visible within a fraction of milliseconds after contact is established and are in the form of Thoroddsen bubbles, sometimes accompanied by Oguz-Prosperetti bubble rings. As visualized in figure 2, bubble rings appear as a cloudy line forming an arc around the two larger bubbles.
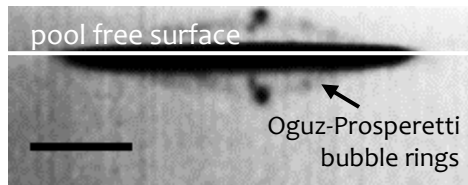

Figure 2. *Initial contact I regime.* Oguz-Prosperetti bubble rings formed in conjunction with Thoroddsen bubbles (Fr = 18, We = 26). Frame acquired at t = 0.8 ms after impact. Scale bar = 1 mm.

The frames reported in figure 3 show the subsequent evolution of the impact process. Following the rupture of the air disk, the liquid of the drop merges with the target fluid and a crater, or cavity, forms. The crater expands changing its initial profile, forced by the flow field induced in the liquid pool: sharp corners develop at the sides of the cavity, while the bottom progressively assumes the shape of a rounded tip as a result of the convergence of a capillary wave. A few milliseconds after impact, the crater reaches its maximum expansion and the surrounding fluid starts to contract the crater. In this regime, the bottom peak rapidly retracts without leaving any bubble. Simultaneously to crater collapse, a smooth bulge rises just above the pool surface and the free surface gradually restores its initial form. Sometimes, a faster rebounding of the crater tip results in the formation of a thicker column of liquid. Small secondary droplets may detach from the liquid column due to capillary instabilities. Those droplets can reach great heights before falling back on the pool surface; however, their size is too small to give rise to any relevant phenomena.

3.1.2. Single bubble I regime. Thoroddsen bubbles are not an exclusive feature of the "*initial contact I regime*". They have been observed for almost the totality of the impact conditions explored in this study. In the regime designated here as "*single bubble I*", their production is followed by the entrainment of one large bubble derived by cavity collapse.

As it can be observed in figure 4.a, in this case the initial profile of the crater is nearly hemispherical as a consequence of the high energy of the impacting drop. When the cavity stops growing downward (t = 19.0 ms after impact), an axisymmetric inward flow develops just above the cavity base [14]. This causes the cavity sidewalls to be pushed inward, while the cavity floor stagnates. Hence, a nipple-like protrusion, visible at t = 21.6 ms, is formed at the base of the cavity. Finally, a capillary wave converging towards the cavity bottom makes the opposite sides of the channel to come into contact before the protrusion can retract. As a consequence, the bottom portion of the cavity is disconnected from the rest of the crater, resulting in the entrainment of a macroscopic bubble in the liquid.
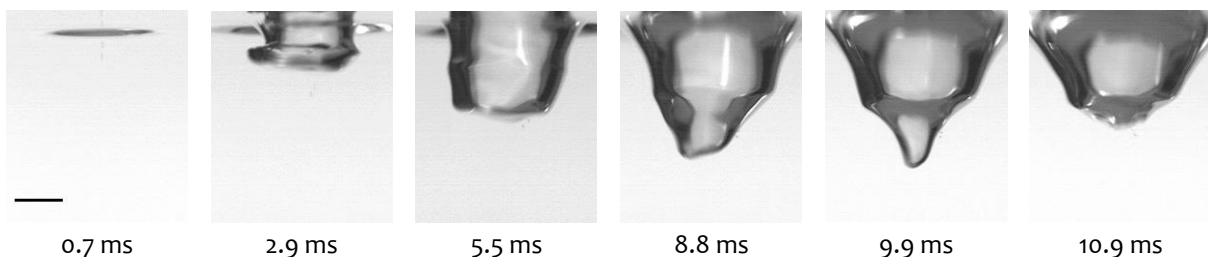

| 0.7 ms | 2.9 ms | 5.5 ms | 8.8 ms | 9.9 ms | 10.9 ms |

Figure 3. *Initial contact I regime.* Image sequence captured below the pool surface (Fr = 60, We = 48, framing rate = 2740 fps). Scale bar 1.5 mm. Times referred to the instant of the first contact.
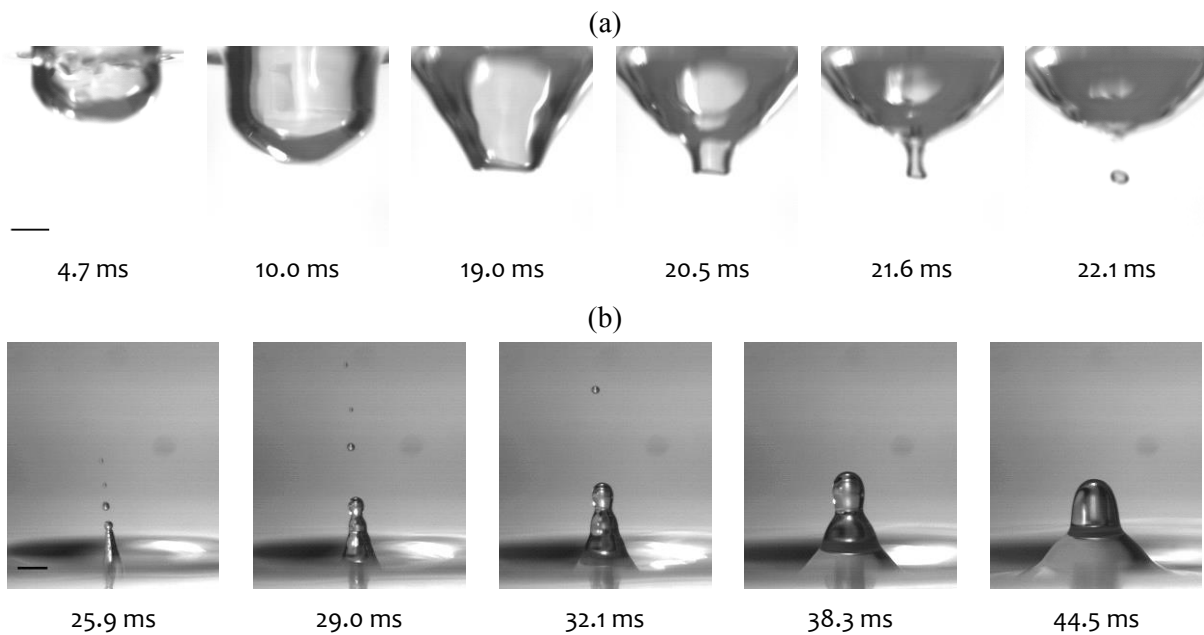
(a)

| 4.7 ms | 10.0 ms | 19.0 ms | 20.5 ms | 21.6 ms | 22.1 ms |

(b)

| 25.9 ms | 29.0 ms | 32.1 ms | 38.3 ms | 44.5 ms |

Figure 4. *Single bubble I regime*. Image sequence captured below (a) and above (b) the pool surface (Fr = 87, We = 133, framing rate = 1898 and 967 fps respectively). Scale bar 2 mm.

The inward axisymmetric flow which governs the crater collapse is responsible also for the formation of an upward liquid jet above the liquid surface [19]. In the "*single bubble I regime*", a short and narrow jet appears, together with a series of small droplets ejected from its tip at high velocity. This situation is illustrated in figure 4.b. The jet quickly reaches a maximum height comparable to the diameter of the primary drop, then starts to thicken and finally subsides.

3.1.3. Single bubble II regime. For a narrow range of Weber and Froude numbers just above the region of the "*single bubble I regime*", a different jet behaviour is encountered in conjunction with the entrainment of the large bubble.

The development of the impact crater is similar to the one observed in the previous regime. Surface tension-driven instabilities may be generated at the bottom of the retracting protrusion, which takes the shape of a slightly curved cylindrical stem. Thus, immediately after detachment, the newly-formed bubble appears to be quite stretched as an effect of stem deformations. However, the most distinctive feature of the "*single bubble II regime*" is the subsequent flow dynamics above the free surface.

Supported by the high potential energy stored in the crater, the jet rises well above the pool surface, preceded by a finite number of very small-sized drops (figure 5).
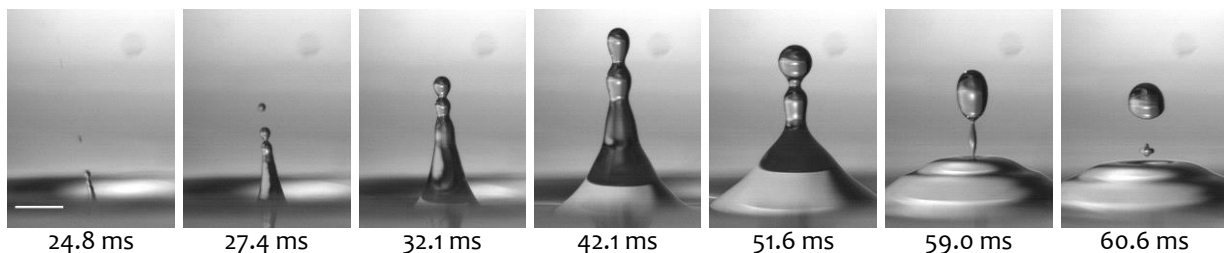

| 24.8 ms | 27.4 ms | 32.1 ms | 42.1 ms | 51.6 ms | 59.0 ms | 60.6 ms |

Figure 5. *Single bubble II regime*. Image sequence captured above the pool surface (Fr = 110, We = 158, framing rate = 1898 fps). Scale bar 3 mm.

The jet body becomes thicker while it continues to rise and its upper portion undergoes severe surface distortions, driven by capillary waves travelling down the jet. Those disturbances are generated during the detachment of the first series of droplets. When the liquid column collapses, the fluid progressively necks until a large drop separates. In the specific sequence shown, a smaller satellite droplet also generates. The large secondary drop is comparable in size to the original impacting drop but has a lower velocity. Drops produced with this mechanism can potentially participate in the introduction of gaseous nuclei when falling back into the pool, as from [11, 20]. A more accurate analysis of the role of the secondary drops on entrainment is left for future analysis.

3.1.4. Multiple bubbles regime. At even higher Weber and Froude numbers ($100 < Fr < 220$, $160 < We < 210$), two or more bubbles are entrained in the liquid pool as a consequence of crater collapse. It is worth to point out, however, that we included under the same category regimes characterised by different nature, variable with the size of the entrained bubbles and the shape of the cavity bottom at pinch-off.

These forms of entrainment are obtained when the surface instabilities established at the floor of the cavity are strong enough to break up the stem structure at multiple locations. Consequently, bubbles similar to the ones shown in figure 6 are produced. The development of the upward moving jet, instead, is identical to the one described in section 3.1.3: after the jet has reached its maximum height, one or, more rarely, two large secondary drops detach from the jet body at the point of large curvature.

3.1.5. Initial contact II regime. When the falling velocity and the size of the primary drop are sufficiently high, the production of bubbles by crater collapse is suppressed. On the contrary, Thoroddsen bubbles are still formed at the very beginning of the impact process. Hence, this last class of events is under many aspects similar to the "*initial contact I regime*" for what concerns the entrainment mechanisms involved in the primary impact. The main differences reside in the dynamics followed by the impact crater (figure 7.a) and the jet (figure 7.b).

In the region referred to as "initial contact II regime", the lateral expansion of the primary impact crater is less limited than in previous regimes as inertial forces dominate and surface tension is not able to restrict the cavity growth. The effect of radial focusing of the flow on crater collapse is also weaker: the base of the cavity reverses its motion before any capillary wave travelling downward the crater walls reaches the bottom. Even the smaller disturbances covering its floor do not have sufficient time to develop before contraction occurs. As a result, no bubbles are detached from the base of the primary crater. In addition, the rapid contraction of the crater gives origin to a thicker, but higher and slower jet than in the previous cases. One or more large drops detach while the jet is still growing. These rise further above the free surface before falling back.
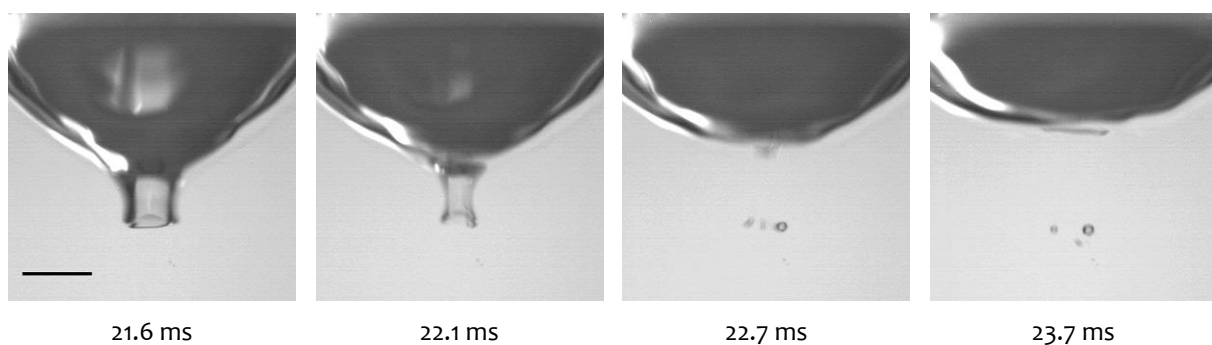

21.6 ms   22.1 ms   22.7 ms   23.7 ms

Figure 6. *Multiple bubbles regime*. Image sequence captured below the pool surface ($Fr = 171$, $We = 196$, framing rate = 1898 fps). Scale bar 2 mm.
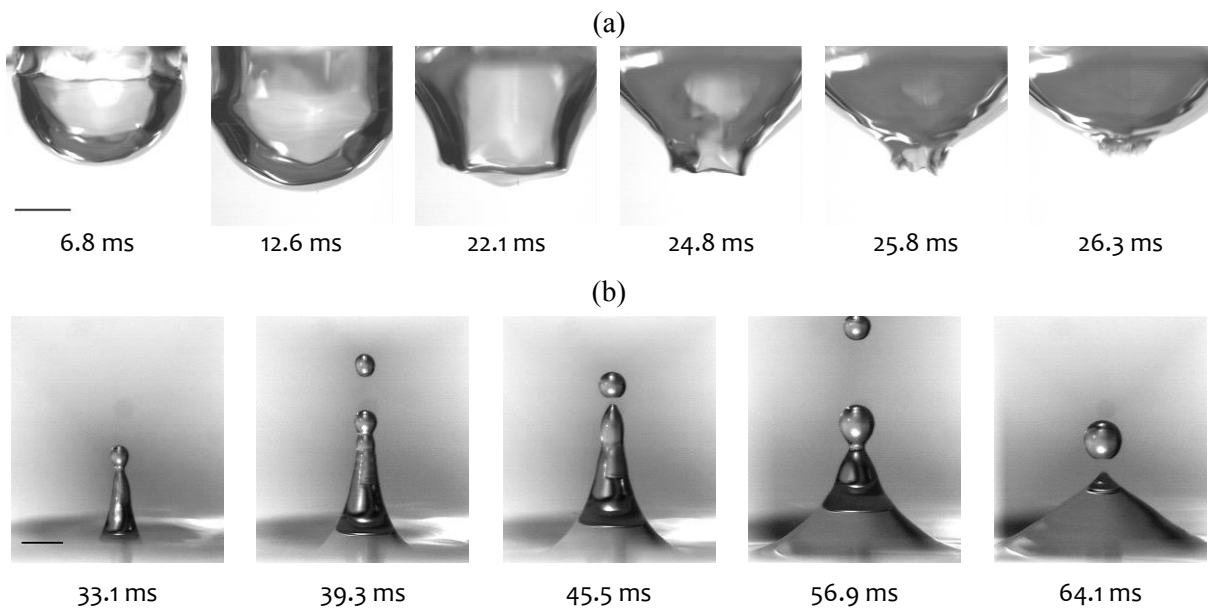
(a)

| 6.8 ms | 12.6 ms | 22.1 ms | 24.8 ms | 25.8 ms | 26.3 ms |

(b)

| 33.1 ms | 39.3 ms | 45.5 ms | 56.9 ms | 64.1 ms |

Figure 7. *Initial contact II regime*. Image sequence captured below (a) and above (b) the pool surface (Fr = 172, We = 247, framing rate = 1898 and 967 fps respectively). Scale bar 3 mm.

3.2. Phase diagram

The conditions under which the entrainment regimes observed in the present work occur, are represented in the Froude-Weber phase diagram displayed in figure 8. Boundaries reported by the literature between regions characterised by distinct forms of entrainment and data acquired by different authors [11, 14] are also plotted.
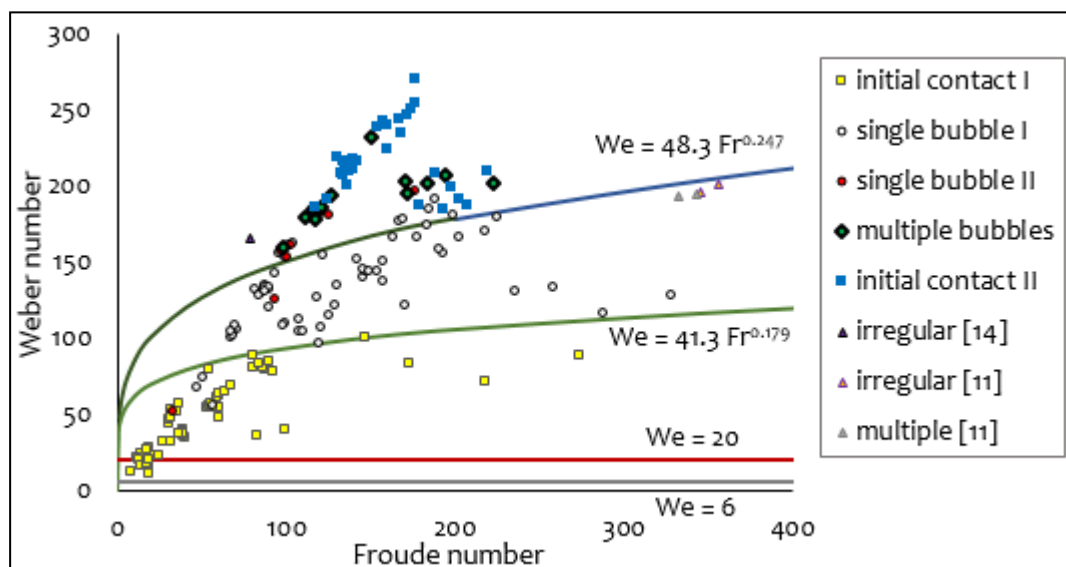

Figure 8. Phase diagram of the entrainment regimes.

The diagram shows that the data acquired herein on *single bubble I regime* fall in the large majority between the curves provided by Oguz and Prosperetti [13], which delimit the region of regular entrainment. Out of this region, results relative to the formation of the single large bubble without large secondary drops are obtained occasionally but are surrounded by points pertaining to different regimes. This implies that a slight change in the impact conditions results in a completely different outcome. Such a behaviour gives a direct confirm of the lack of reproducibility typical of this entrainment mechanism for We and Fr values above and below the two reference curves.

The region below the lower boundary of regular entrainment is dominated by the *initial contact I regime*. The introduction of gaseous nuclei in the form of Thoroddsen bubbles is encountered also for Weber values lower than 20, that is, below the limit determined by Thoroddsen et al. [10] and by Liow and Cole [11]. According to Liow and Cole, Mesler entrainment should, instead, take place for 6 < We < 20. A possible explanation of this discrepancy may reside in the variability typical of Mesler entrainment in water: at parity of conditions, the presence of surface contaminants or even a small deviation in the shape of the drop may hinder the formation and rupture of the hemispherical air film [2, 21]. For a narrow subset of Froude and Weber numbers in the region of *initial contact I regime* (8 < Fr < 32, 10 < We < 32), Oguz-Prosperetti bubble rings have been observed in conjunction with Thoroddsen bubbles. It is not clear if their disappearance for We and Fr > 32 is determined by a suppression of the mechanisms of their production, or if their size becomes so small that they escape detection with the imaging system adopted.

The formation of Thoroddsen bubbles in the absence of other entrainment mechanisms from the primary drop is achieved also at We and Fr numbers above the upper limit of regular entrainment. In that region, large secondary drops are usually pinched-off from the jet emerging after cavity retraction. Their effect in the introduction of gaseous nuclei needs to be ascertained. For We > 210, the *initial contact II regime* takes place systematically, but the data collected are too scant to determine the trend of occurrence of this phenomenon. For Weber numbers lower than 210 and higher than the upper limit of regular entrainment, the *initial contact II regime* mixes up with different mechanisms of entrainment, involving the production of one or more bubbles by crater collapse. *Multiple bubbles regime* is, in general, obtained at We and Fr numbers higher than those typical of *single bubble I and II regimes*, in the range that we provisionally established to be 100 < Fr < 220 and 160 < We < 210. This suggests that, above a certain threshold, surface tension forces are no longer able to contain the crater expansion. However, the definition of the quantitative limits of occurrence of multiple entrainment is rather difficult, since these data are not grouped in a well-delimited region. The present results offer a much richer phase-diagram than the available counterparts in the literature, but further work is required to ascertain if the region exhibiting mixed forms of entrainment is characterised by intrinsic instabilities or if other factors come into play in determining the impact behaviour.

3.3. Size and residence time of the entrained bubbles

As discussed in the previous sections, a large variety of bubbles can be introduced in the liquid pool as a result of drop impacts. Their properties and behaviour depend on the particular mechanism leading to their production.

Thoroddsen bubbles have been detected almost in the totality of impact events, with measured diameters ranging between 0.026 and 0.145 mm. After formation, these nuclei propagate ahead of the expanding impact crater and can be carried deeper into the liquid bulk by vortex rings. Alternatively, they can be drawn into the cavity wake and pulled towards the free surface when the cavity retracts. In both cases, Thoroddsen bubbles are retained in the liquid for long times: increasing the acquisition time of the cameras made it possible to observe that these nuclei were still present about 15 seconds after impact.

As opposite, Oguz-Prosperetti bubble rings disappear a few milliseconds after their formation. It is not clear if this is due to a rapid dissolution of these nuclei in the liquid, or to their outward motion from the impact point, which drives them out of the plane of focus. Bubbles in this category are too small to be resolved with the imaging system adopted in the present experiments, which offers a

magnification of 23 μm/pixel. Hence, quantitative information about their exact number and size can not be extracted by the images herein acquired.

Single bubbles entrained by cavity collapse have sizes covering a wide range of values: diameters ranging between 0.07 and 1.22 mm have been found across both the *single bubble I* and *II regimes*. Bubbles of this kind, once released, can move further downward in the liquid, as a consequence of the slight increase in cavity depth before retraction. In this lapse of time, the bubble oscillates radially, until a spherical shape is assumed. As buoyancy becomes dominant, the bubble reverses its motion and rises towards the free surface. The elasticity of the interface can make the bubble bounce on the free surface for one or more times. Eventually, bubble interface coalesces with the pool surface, leading to bubble collapse. This process usually comes to an end within a fraction of second, residence times up to nearly 0.5 s being typical of nuclei produced by this form of entrainment.

In *multiple bubbles regime*, from a minimum of 2 to a maximum of 6 bubbles have been obtained, depending on the peculiar development of capillary instabilities on the cavity floor. In the cases where two bubbles are formed, their diameter is usually of the order of 400 μm. After detachment, the bubbles move deeper into the liquid bulk, until the buoyancy force drives them towards the free surface where they burst nearly immediately (at about 0.6 s after their formation). When three or more bubbles are produced, the size of the gaseous nuclei is usually smaller, and diameters ranging between 26 and 280 μm have been measured. Such small bubbles are less affected by buoyancy and they continue their downward motion into the fluid, until they exit from the field of view and no longer re-appear.

4. Conclusions

Through an extensive experimental campaign, the effect of drop impacts on the population of gaseous nuclei inside a liquid pool was investigated. The analysis of the impact events, performed with the use of high-speed imaging, has revealed the existence of five distinct entrainment regimes, on-setting at different impact conditions. Those regimes have been classified on the basis of the mechanisms taking part in the bubble production process. The fluid dynamics typical of each regime was discussed, after collecting and analysing high-speed image sequences for 176 drop impacts.

The conditions of occurrence of the entrainment regimes were summarized on a Froude-Weber phase diagram. The present data largely confirm the results reported in the literature, showing the existence of well-delimited entrainment regions. In addition, fresh data on *initial contact II*, *single bubble II* and *multiple bubbles regimes* have been provided, thus contributing to complete the scenario of drop-impact regimes. The results also highlight the presence of undefined entrainment regions, whose understanding requires further analysis.

In addition, the size and the behaviour of the entrained nuclei have been characterised in order to assess the incidence of bubble entrainment in practical applications. The data provided help to clarify the role played by bubble entrainment in real-world processes. These, however, require the investigation of additional effects, such as the interaction with solid walls and secondary impacts.

References

[1]   Wanninkhof R, Asher W E, Ho D T, Sweeney C and McGillis W R 2009 *Ann. Rev. Mar. Sci.* **1** 213–44
[2]   Esamilizadeh H and Mesler R 1986 *J. Colloid Interface Sci.* **110** 561–74
[3]   Sigler J and Mesler R 1990 *J. Colloid Interface Sci.* **134** 459–74
[4]   Li H, Mei S, Wang L, Gao Y and Liu J 2014 *Int. J. Heat Fluid Fl.* **47** 1–8
[5]   Saeedipour M, Schneiderbauer S, Pirker S and Bozorgi S 2014 *Magnesium Technology* ed M Alderman, M V Manuel *et al* (Hoboken: John Wiley & Sons) pp 185–90
[6]   Lin T J 1971 *J. Soc. Cosmet. Chem.* **22** 323–37
[7]   Ashurst P R 2005 *Chemistry and Technology of Soft Drinks and Fruit Juices* (Oxford: Blackwell Publishing Ltd)
[8]   Thoroddsen S T, Thoraval M-J, Takehara K and Etoh T G 2012 *J. Fluid Mech.* **708** 469–79

[9]   Tran T, de Maleprade H, Sun C and Lohse D 2013 *J. Fluid Mech.* **726** R3
[10]   Thoroddsen S T, Etoh T G and Takehara K 2003 *J. Fluid. Mech.* **478** 125–34
[11]   Liow J-L and Cole D E 2007 Bubble entrapment mechanisms during the impact of a water drop
           Proc. 16th Australasian Fluid Mechanics Conf. pp 866–69
[12]   Oguz H N and Prosperetti A 1989 *J. Fluid Mech.* **203** 149–71
[13]   Oguz H N and Prosperetti A 1990 *J. Fluid Mech.* **219** 143–79
[14]   Elmore P A, Chahine G L and Oguz H N 2001 *Exp. Fluids* **31** 664–73
[15]   Deng Q, Anilkumar A V and Wang T G 2007 *J. Fluid Mech.* **578** 119–38
[16]   Pumphrey H C, Crum L A and Bjørnø L 1989 *J. Acoust. Soc. Am.* **85** 1518–26
[17]   Franz G J 1959 *J. Acoust. Soc. Am.* **31** 1080
[18]   Liow J-L 2001 *J. Fluid Mech.* **427** 73–105
[19]   Rein M 1996 *J. Fluid Mech.* **306** 145–65
[20]   Carroll K and Mesler R 1981 *AIChE J.* **27** 853–55
[21]   Mills B H, Saylor J and Testik F Y 2012 *AIChE J.* **58** 46–58